Available online at www.sciencedirect.com
SCIENCE DIRECT®
Journal of Solid State Chemistry 178 (2005) 800–810
JOURNAL OF SOLID STATE CHEMISTRY
www.elsevier.com/locate/jssc

Solid solubilities of $(La\ Nd,)_2(Zr,Ti)_2O_7$ phases deduced by neutron diffraction

Elizabeth J. Harvey[a], Karl R. Whittle[a], Gregory R. Lumpkin[a], Ronald I. Smith[b], Simon A.T. Redfern[a,*]

[a]*Department of Earth Sciences, University of Cambridge, Downing Street, Cambridge CB2 3EQ, UK*
[b]*ISIS Facility, Rutherford Appleton Laboratory, Oxon OX11 OQX, UK*

Received 6 October 2004; received in revised form 3 December 2004; accepted 17 December 2004

Abstract

Time-of-flight powder neutron diffraction has been performed on oxides with composition $(La_{1-x}Nd_x)_2Zr_2O_7$ and $Nd_2(Zr_{1-x}Ti_x)_2O_7$, where $x = 0$, 0.2, 0.4,…1.0, in order to determine the solid solution behaviour across each series. Between $La_2Zr_2O_7$ and $Nd_2Zr_2O_7$, a cubic pyrochlore phase is observed ($Fd\bar{3}m$, $Z = 8$). A linear decrease in the lattice parameter from 10.8047 to 10.6758 Å indicates complete miscibility of the two end-members. For the same series, the 48*f* oxygen *x*-parameter increases from 0.3313 to 0.3348, suggesting increased distortion of the 6 coordinate *B* sites and reduced distortion of the 8 coordinate *A* sites. There is limited solubility of $Nd_2Ti_2O_7$ in $Nd_2Zr_2O_7$. Exsolution of a monoclinic phase ($P2_1$, $Z = 8$) rich in $Nd_2Ti_2O_7$ is observed at approximately $x = 0.56$. The compositional range over which a solid solution exists is more extensive than that which has been previously reported. The solubility of $Nd_2Zr_2O_7$ in $Nd_2Ti_2O_7$ is very low.

Keywords: Pyrochlore; Neutron diffraction; Solid solution

1. Introduction

Crystalline materials with the pyrochlore structure have been suggested as candidates for the immobilisation of actinide species found in high-level nuclear waste (HLW) streams from the nuclear power industry and weapons decommissioning programmes. The introduction of pyrochlore to Synroc [1] phase assemblages tailors them for direct waste loading of actinide-rich fuel elements [2,3]. The resilience of crystalline ceramics, such as these, to intrinsic radiation damage and degradation by repository groundwater is likely to far exceed that of the borosilicate glasses currently employed for immobilisation [4].

The pyrochlore structure $A_2B_2O_6X$, (space group $Fd\bar{3}m$, $Z = 8$) is an ordered superstructure of fluorite with a cubic lattice parameter of about 10 Å, roughly twice that of fluorite (see Fig. 1). The *A*-cations (typically rare earths) occupy 16*d* Wyckoff positions $(\frac{1}{2},\frac{1}{2},\frac{1}{2})$, whilst *B*-cations (Zr, Ti) reside on 16*c* sites (0,0,0). Relative to fluorite, one-eighth of the anions have been removed in an ordered manner, producing an unoccupied site (8*a*, $(\frac{1}{8},\frac{1}{8},\frac{1}{8})$). Six of the seven anions per formula unit of pyrochlore reside in 48*f* positions $(x,\frac{1}{8},\frac{1}{8})$, with $x \sim \frac{3}{8}$ which relax towards the unoccupied 8*a* sites. The remaining anion occupies 8*b* positions $(\frac{3}{8},\frac{3}{8},\frac{3}{8})$. The magnitude of the 48*f* oxygen relaxation depends on the types of cations, 8*b* anions and site occupancies and is indicated by the 48*f* *x*-positional parameter—the only variable atomic coordinate within the pyrochlore structure. This parameter, which can theoretically take values from 0.3125 to 0.375 [5], affects the local coordination geometry around *A* and *B* cations. The geometry of the 8 coordinate *A* sites changes from scalenohedral with 6 + 2 local coordination, to that of a

*Corresponding author. Fax +44 1223 333450.
E-mail address: satr@cam.ac.uk (S.A.T. Redfern).

0022-4596/$ - see front matter © 2004 Elsevier Inc. All rights reserved.
doi:10.1016/j.jssc.2004.12.030

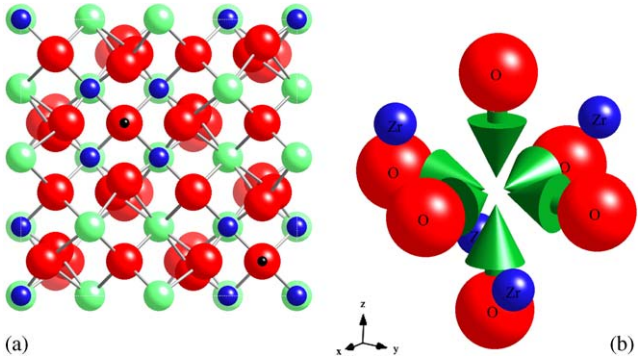

Fig. 1. (a) One Unit cell of the pyrochlore structure projected down [001]. The large, dark grey spheres (red online) are oxygen atoms. Cations on the 16*d* positions (8-fold coordinated) are medium sized and light coloured (green online); those on the 16*c* sites (6-fold coordinated) are smaller and dark grey (blue online). The small black unbonded spheres indicate the position of unoccupied 8*a* sites. (b) Relaxation of the 48*f* oxygens towards the vacant 8*a* site. The magnitude of this relaxation increases with increasing La content in $(La_{1-x}Nd_x)_2Zr_2O_7$ pyrochlores.

regular cube, whilst the 6 coordinate octahedral geometry of *B* sites distorts from octahedral to a trigonal antiprism as x increases to 0.375.

The beauty of the pyrochlore system lies in its ability to incorporate an incredibly diverse range of elements, usually by combining 2+/5+ or 3+/4+ cations on the *A* and *B* sites, respectively, in proportions such that the average ionic radius ratio of cation sites (r_A/r_B) lies within the pyrochlore stability field. Subramanian et al. [5] report that pyrochlore structures are formed when r_A/r_B lies between 1.46 and 1.78. Defect fluorite structures are produced when r_A/r_B falls below this range, whilst at higher values, the stable structure is monoclinic.

As a result of the compositional diversity, the electrical, thermal, magnetic and luminescent properties of pyrochlores are highly variable, and materials with this structure have been reported with a range of potential technological applications [5–9]. U, Pu, and Th have all been incorporated into pyrochlores [10–12], and the structure has been shown to have good resistance to radiation damage [13,14].

Synthetic and natural titanate minerals have been the focus of much of the research into ceramics for the immobilisation of radioactive nuclei. Titanates generally have a very low aqueous solubility, and the variable Ti oxidation state allows the incorporation of relatively high levels of impurities, without the formation of secondary phases. However, the resistance of such minerals to damage by radiation is often very low [15]. Substitution of Ti by Zr can yield materials that are far more radiation resistant, at the expense of reduced structural flexibility and higher processing temperatures [16].

Here we explore the solid solution behaviour of Ti and Zr in a pyrochlore system, deduced by neutron diffraction, to assess whether the two species can be used in conjunction, to produce a single phase pyrochlore which could combine the properties associated with titanates and zirconates. An investigation of some zirconotitanate systems by X-ray diffraction has been previously undertaken by Shoup et al. [17]. They report that the limit of Ti solubility in $Nd_2(Zr_{1-x}Ti_x)_2O_7$ with the pyrochlore structure lies at about $x = 0.43$; increasing the proportion of Ti beyond this results in exsolution of a Ti-rich monoclinic phase.

Given the problems associated with studying radioactive samples, rare-earth elements are often employed as non-radioactive analogues of actinide elements. Adopting this approach, variation in the pyrochlore structure between $La_2Zr_2O_7$ and $Nd_2Zr_2O_7$ end members has also been investigated. The average *A* site cation ionic radii can be used to make predictions about the behaviour of the crystal structure under different potential waste loadings of Pu, U or Am.

2. Experimental

Ceramics with composition $Nd_2(Zr_{1-x}Ti_x)_2O_7$ and $(La_{1-x}Nd_x)_2Zr_2O_7$ ($x = 0$, 0.2, 0.4, 0.6, 0.8, 1.0) were prepared by conventional mixed metal-oxide methods. Stoichiometric mixtures of La_2O_3, Nd_2O_3, TiO_2 (rutile) and ZrO_2 (Aldrich, 99.5%) were ground as acetone slurries (50% volume solids), for 30 min, followed by drying at ~120 °C. Cold uniaxial pressing at 200 bar was used to produce pellets with diameter 8 mm, height ~10 mm. These were heated to 1500 °C at a rate of 5 °C min^{-1} and calcined in air at this temperature for 48 h before cooling at up to 50 °C min^{-1}. Grinding, pressing and sintering were repeated once to improve sample homogeneity. Calcined zirconates varied in colour from cream to pale blue with increasing Nd, whilst increasing the proportion of Ti in $Nd_2(Zr_{1-x}Ti_x)_2O_7$ created dark grey-purple pellets with a large reduction in size during sintering. Preliminary powder X-ray diffraction confirmed the presence of the expected cubic and/or monoclinic phases, with no impurities.

For neutron diffraction experiments, approximately 15 g of each powdered sample were loaded into thin-walled cylindrical vanadium sample cans. The cans were mounted in an automatic sample changer, which was placed in the sample chamber of the high flux neutron time-of-flight (TOF) powder diffractometer POLARIS, at the ISIS pulsed spallation neutron source, Rutherford Appleton Laboratory, UK, [18]. Each sample was run at room temperature for a total integrated proton beam current to the ISIS target of 100 μA h (about 40 min) and data were collected over a TOF range of 1500–19600 μs, corresponding to d spacings between 0.25 and 3.2 Å. Data were recorded by a bank of 58 ^{3}He gas tube detectors positioned at average $2\theta = 145°$. The data

from each tube were individually converted to *d* spacing, rebinned and then summed. An empty instrument background was subtracted and the data were normalised using an incoherent scattering pattern from a vanadium sample. Instrument parameters were refined at the start of the experimental cycle using diffraction from an NBS Si sample.

The diffraction profiles were fitted by the Rietveld method [19], using the general structure analysis system (GSAS) [20], with the front-end graphical user interface 'EXPGUI' [21]. Full pattern analysis was undertaken, refining the structure using space groups $Fd\bar{3}m$ and $P2_1$. All structural models were refined to convergence. All atoms in the pyrochlore structure are located on high symmetry special positions in the space group $Fd\bar{3}m$, with their coordinates fixed by symmetry, with the exception of the 48*f* oxygen *x*-parameter. Throughout this report, a *B* cation was placed on the origin of the unit cell (the 16*c* site in $Fd\bar{3}m$, origin choice 2), in accordance with Subramanian et al. [5] and Tabira and Withers [22]. Where samples consisted of a single cubic phase, profile refinement included six background parameters (fitted to a shifted Chebyschev polynomial), scaling, one cell parameter, four profile parameters and 5–7 structural parameters (including 48*f* oxygen *x*-position, isotropic temperature factors and fractional occupancies between cations on the same crystallographic positions, e.g. La and Nd for $(La_{1-x}Nd_x)_2Zr_2O_7$ and Zr and Ti for $Nd_2(Zr_{1-x}Ti_x)_2O_7$). Total refinement of cation exchange across available sites was not possible, for reasons outlined by Heremans et al. [23]. Thus, we used a model in which the 16*c* position is fully occupied by Zr in $(La_{1-x}Nd_x)_2Zr_2O_7$ and the 16*d* position is fully occupied by Nd in $Nd_2(Zr_{1-x}Ti_x)_2O_7$. Similar parameters were refined for monoclinic phases with an increase to four cell parameters.

Constraints were added to ensure the stable refinement of structural models. If two atom types resided on a single crystallographic site, the atoms were constrained to have the same positional and thermal parameters, and fractional occupancy parameters totalling unity. For monoclinic phases, all atoms occupying similar sites (i.e. all Nd, all Zr and Ti and all O) were constrained to have the same thermal parameters. For biphasic and monoclinic diffraction patterns, a LeBail fit was first undertaken (refining background, cell, peak profile, and peak intensity in the absence of a structural model), before a full Rietveld analysis was implemented as described above.

Fragments of sintered pellets were analysed on a Jeol JSM-820 scanning electron (BSE) microscope (SEM) equipped with an X-ray energy dispersive unit and operating at an accelerating voltage of 20 kV. The resin-mounted samples were polished (using 1 μm diamond grit as final abrasive), before the surfaces were coated with a conducting layer of carbon approximately 20 nm thick. The same samples were also analysed using a Cameca-SX100 Electron Probe Microanalyser, operating at an accelerating voltage of 20 kV and a current of 20 nA, with a beam diameter of 1 μm. Backscattered images were employed during electron probe microanalysis (EPMA), in order to distinguish between different phases.

3. Results and discussion

3.1. Structural variations across the solid solution $(La_{1-x}Nd_x)_2Zr_2O_7$

The results of Rietveld profile refinements for the $(La_{1-x}Nd_x)_2Zr_2O_7$ series are presented in Table 1. An example of a profile refinement, showing the goodness of fit obtained is given in Fig. 2. Here, a calculated pattern (solid line) has been fitted to measured data points (crosses). The difference between the experimental data and calculated fit is displayed below these and indicates a very good fit to the data. The dashed lines indicate expected peak positions in the calculated profile.

Powder diffraction patterns for $(La_{1-x}Nd_x)_2Zr_2O_7$ are shown in Fig. 3. The presence of cubic reflections, particularly the [331] reflection at similar intensity throughout these patterns, indicate that all compositions investigated within this series, crystallise in the pyrochlore structure, with a cubic unit cell edge twice that of the fluorite structure from which it can be described. Compositional changes across the solid solution have an obvious effect on the cell parameters. Pyrochlore reflections occur at decreasing TOF (or *d* spacing) values, as a function of increasing Nd content (ionic radius of La^{3+} (8 coordinate.) = 1.16 Å, Nd^{3+} (8 coordinate.) = 1.109 Å [24]). This leads to a reduction in the unit cell size. The decrease is linear (as shown in Fig. 4a), with only one phase present for all compositions. This behaviour, in accordance with Vegard's law, suggests that mixing is near ideal across this range of compositions, indicative of complete solubility of $La_2Zr_2O_7$ in $Nd_2Zr_2O_7$.

Results presented here for the cell parameter of $La_2Zr_2O_7$ lie between those reported by Tabira et al. [25] and Whittle et al. [26]; given as 10.7997 and 10.8102 Å, respectively. Given the realistic accuracy (rather than precision) of the cell parameter refinements in each case, which is reasonably of the order of 0.001 Å, these values may be considered as in agreement within error. Our reported cell parameter for $Nd_2Zr_2O_7$ agrees well with that of van Dijk et al. [27] (10.676 Å), although there is less agreement between the two 48*f* oxygen *x*-parameters, probably because van Dijk et al.'s study used X-rays, which are less sensitive for the measurement of oxygen in the presence of heavy ions.

Table 1
Refined parameters for $(La_{1-x}Nd_x)_2Zr_2O_7$, $x = 0$, 0.2, 0.4, 0.6, 0.8, 1

Ideal composition	R_{wp} (%)	Lattice parameter (Å)	48*f* oxygen *x*-parameter	Fraction Nd on *A* site	*A* site B_{iso} (Å^2)	Zr B_{iso} (Å^2)	O(48*f*) B_{iso} (Å^2)	O(8*b*) B_{iso} (Å^2)
$La_2Zr_2O_7$	2.02	10.80470(6)	0.331(3)	0.0	0.610(6)	0.416(6)	0.702(5)	0.50(1)
$La_{1.6}Nd_{0.4}Zr_2O_7$	2.05	10.78457(2)	0.33179(2)	0.26(4)	0.631(7)	0.447(6)	0.732(5)	0.562(9)
$La_{1.2}Nd_{0.8}Zr_2O_7$	1.88	10.75648(2)	0.33244(2)	0.37(4)	0.655(7)	0.453(6)	0.754(5)	0.590(9)
$La_{0.8}Nd_{1.2}Zr_2O_7$	2.15	10.72892(3)	0.33308(3)	0.50(5)	0.671(9)	0.467(7)	0.788(6)	0.58(1)
$La_{0.4}Nd_{1.6}Zr_2O_7$	1.93	10.70252(3)	0.33382(3)	0.55(4)	0.679(8)	0.466(6)	0.804(6)	0.53(1)
$Nd_2Zr_2O_7$	1.24	10.67587(3)	0.33481(3)	1.0	0.608(7)	0.529(7)	0.869(6)	0.44(1)

Figures in parentheses show the standard deviation (as the error in the last digit).
*Analysed compositions (by EPMA) for ideal $x = 0.6$ and 0.8 are $La_{0.74}Nd_{1.18}Si_{0.03}Zr_2O_7$ and $La_{0.38}Nd_{1.55}Si_{0.04}Zr_2O_7$, respectively.

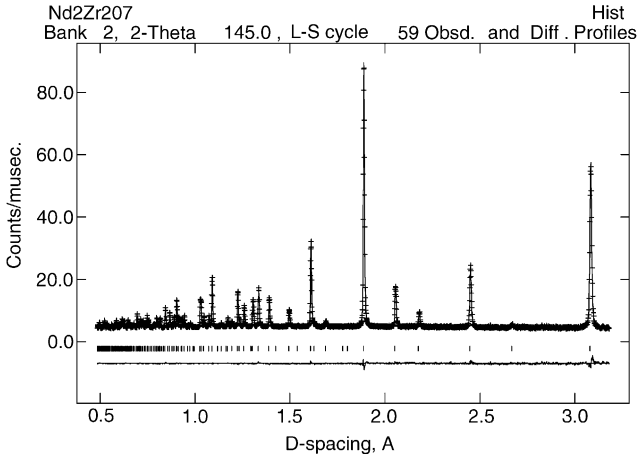

Fig. 2. Fitted TOF powder diffraction pattern for $Nd_2Zr_2O_7$. Experimental data are shown as crosses, the solid line is the Rietveld fit to the data. Vertical bars represent the positions of calculated reflections. The bottom line shows the difference between measured data and calculated fit.

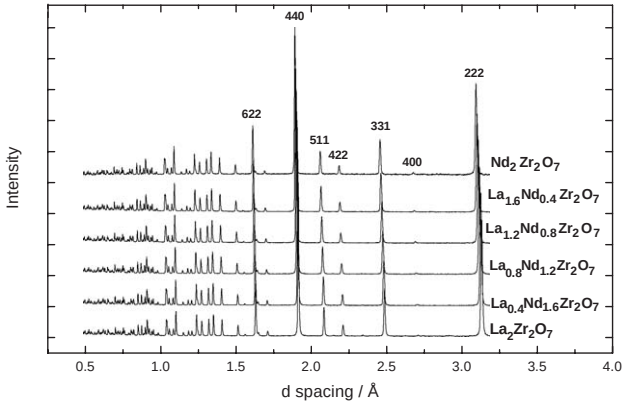

Fig. 3. TOF neutron powder diffraction patterns for the solid solution series $(La_{1-x}Nd_x)_2Zr_2O_7$. *hkl* indices of some pyrochlore reflections are given.

The refined 16*d* site occupancies are mostly similar to those expected based on the ideal stoichiometric compositions. However, there are some discrepancies, particularly for $La_{0.8}Nd_{1.2}Zr_2O_7$ and $La_{0.4}Nd_{1.6}Zr_2O_7$,

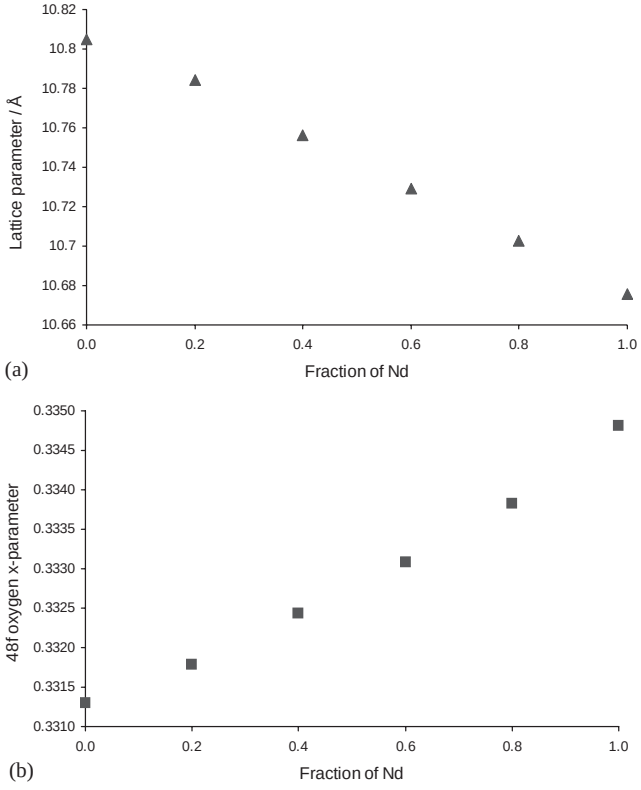

Fig. 4. (a) Lattice parameter and (b) 48*f* oxygen *x*-positional parameter for $(La_{1-x}Nd_x)_2Zr_2O_7$. Error bars are smaller than the size of the symbols.

where the values are lower than expected. EPMA suggests compositions much closer to the ideal values. This technique relies on point sampling and is therefore susceptible to small regions of impurities or porosity, unlike the bulk analysis undertaken in powder diffraction. However, in this case, the EPMA analysis is likely to be more accurate. The main reason for this is that the assumption made during powder profile refinements, that no disorder occurs across the *A* and *B* cation sites is potentially inaccurate. Minervini et al. [28] report that a degree of disorder across *A* and *B* sites is essential, in

order to calculate accurate values of the 48*f* oxygen *x*-positional parameter for a range of compositions that show good agreement with experimental data. Having ignored this factor out of necessity, it is not surprising that a degree of inaccuracy has been introduced into the refined site occupancies. It is also worth noting that the similar coherent scattering lengths of La and Nd (8.24 and 7.69 fm, respectively) enhance the difficulty in obtaining an accurate determination, although this factor alone should not be sufficient to produce the discrepancies observed. Note that because of the ambiguity in the true site occupancy values (and hence proportions of La and Nd in the ceramics) the nominal (ideal) values have be used as labels for figures in this report.

Fig. 4b illustrates the increase in 48*f* oxygen *x*-positional parameter, as the proportion of Nd in the solid solution rises. The deviation from linearity observed in the 48*f* *x*-parameters may be related to a small amount of disorder occurring in the pyrochlore structure. According to Minervini et al. [28,29], there is a correlation between cation anti-site disordering and the formation of Frenkel pair defects between a 48*f* oxygen and unoccupied 8*a* position when the two defect types are adjacent to each other. Both have an effect on the lattice parameter and the 48*f* oxygen *x*-parameter, but the latter is reportedly more sensitive to small amounts of disorder. This indication of disorder across sites further suggests that the refined 16*d* site occupancies are not always reliable. The variation of the 48*f* oxygen *x*-parameter, together with the cell parameter variation across the solid solution, also leads to commensurate changes in bond lengths and angles at the *A* and *B* sites. The linear decrease in lattice parameter due to the reduced average size of *A* cations is accompanied by a reduction in *A*–O(48*f*), *A*–O(8*b*) and *B*–O(48*f*) bond lengths, corresponding to reduction in size of the coordination polyhedra in which these cations reside. We note that the *A*–O(48*f*) bond length decreases by around 2.1% on going from $La_2Zr_2O_7$ to $Nd_2Zr_2O_7$, while the *A*–O(8*b*) distance (which only depends on the cell parameter) decreases by only 1.2% between the same two compositions. This is due to the trend (with increasing Nd-content) towards a more regular cubic coordination around A cations (16*d* sites) and an increasing distortion of the 6-coordinate geometry around *B* cations (16*c* sites), towards a more distorted trigonal antiprism.

Fig. 5 shows a typical zirconate sample after two 48 h periods of calcination with regrinding and repressing in between. In general, our zirconate samples were very poorly sintered, with high porosity (around 90% density). Despite this, it can be seen that the matrix ceramic is very homogeneous. EDS confirms this, indicating a uniform composition throughout the sample, although fully quantitative analysis of the data is hampered by the proximity of La and Nd signals, which overlap in the EDS spectra. Some Si impurities were recorded; these were probably incorporated during milling in agate pots as part of the synthesis process.

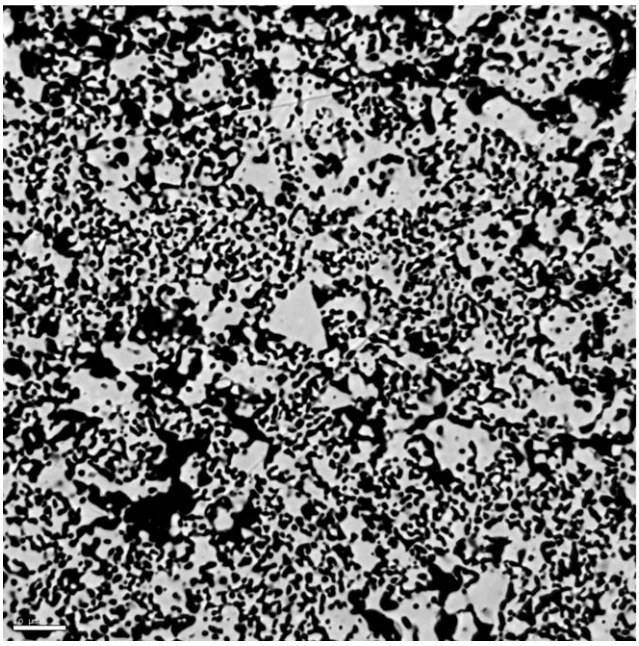

Fig. 5. Backscattered SEM image of $La_{0.8}Nd_{1.2}Zr_2O_7$. The ceramic matrix appears uniformly grey. Dark regions are areas of porosity. Scale bar is 10 μm.

3.2. Structural variations and solid solubility for the series $Nd_2(Zr_{1-x}Ti_x)_2O_7$

Refined parameters for this series are given in Tables 2 and 3. Unlike $(La_{1-x}Nd_x)_2Zr_2O_7$, this series does not represent a complete solid solution of $Nd_2Zr_2O_7$ in $Nd_2Ti_2O_7$ across all compositions. This can be seen upon inspection of Fig. 6, which shows the neutron powder diffraction patterns for compositions across the series and indicates the crystalline phases present.

Between $Nd_2Zr_2O_7$ and $Nd_2Zr_{1.2}Ti_{0.8}O_7$, a single phase with cubic pyrochlore structure is observed. Note particularly, the high intensity (222) and (440) peaks at *d* spacings of 3.1 and 1.85 Å, respectively, and the less intense (331) reflection at 2.45 Å. The intensity of some pyrochlore peaks, for example the (400) peak (labelled * in Fig. 6) increases dramatically as the proportion of Ti is raised. This is due to the effect of the negative coherent scattering length of Ti^{4+} (−3.438 fm) on the total structure factor of the (400) reflection.

At Ti-rich compositions of $Nd_2Zr_{0.8}Ti_{1.2}O_7$ and above, the limit of solid solubility is exceeded and a second crystalline phase with monoclinic structure (space group $P2_1$) is exsolved (see Fig. 7). New peaks are observed in $Nd_2Zr_{0.8}Ti_{1.2}O_7$ at *d* spacings of 2.22,

Table 2
Refined parameters for cubic phases in the series: $Nd_2(Zr_{1-x}Ti_x)_2O_7$, $x = 0$, 0.2, 0.4, 0.6, 0.8

Ideal composition	R_{wp}/%	Lattice parameter (Å)	48*f* oxygen *x*-parameter	Fraction Zr on *B* site	*A* site B_{iso} (Å^2)	*B* site B_{iso} (Å^2)	O(48*f*) B_{iso} (Å^2)	O(8*b*) B_{iso} (Å^2)
$Nd_2Zr_2O_7$	1.24	10.67587(3)	0.33481(3)	1.00	0.608(7)	0.529(7)	0.869(6)	0.44(1)
$Nd_2Zr_{1.6}Ti_{0.4}O_7$	1.66	10.5908(1)	0.33273(4)	0.778(2)	0.72(1)	0.52(2)	1.11(1)	0.44(1)
$Nd_2Zr_{1.2}Ti_{0.8}O_7$	2.38	10.5254(1)	0.33051(4)	0.594(2)	0.80(1)	0.44(2)	1.18(1)	0.48(1)
$Nd_2Zr_{0.8}Ti_{1.2}O_7$	2.36	10.46209(4)	0.32884(5)	0.445(3)	0.80(1)	0.43(4)	1.13(1)	0.50(2)
$Nd_2Zr_{0.4}Ti_{1.6}O_7$	1.46	10.46015(6)	0.32856(6)	0.445(3)	0.983(9)	0.85(9)	1.289(7)	0.73(2)

Figures in parentheses show the standard deviation (as the error in the last digit).

2.30 and 2.68 Å. The intensity of these peaks increases between $Nd_2Zr_{0.8}Ti_{1.2}O_7$ and $Nd_2Zr_{0.4}Ti_{1.6}O_7$, together with the appearance of numerous additional monoclinic reflections, indicating that the overall proportion of this new phase increases substantially. The relatively weak intensity of monoclinic reflections in the powder diffraction pattern of $Nd_2Zr_{0.8}Ti_{1.2}O_7$ suggests that this composition is close to the solid solution limit of $Nd_2Ti_2O_7$ in $Nd_2Zr_2O_7$. Exsolution of the monoclinic phase occurs close to this composition, so the proportion of the second phase is low at this point.

Formation of a second phase occurs because the increasing proportion of Ti leads to a decrease in the average radius of *B* site cations, causing the average cation radius ratio (r_A/r_B) to increase beyond 1.78—the upper stability limit for compositions with the pyrochlore structure [5]. Once the solubility limit of $Nd_2Ti_2O_7$ in $Nd_2Zr_2O_7$ has been reached, excess $Nd_2Ti_2O_7$ is accommodated in a Ti-rich monoclinic phase. When this happens, no further changes in the composition of the cubic phase occur, so the lattice parameter of this phase reaches a plateau (Fig. 8). Before the limit of solid solution is reached, the cubic lattice parameter decreases linearly with increasing Ti, in accordance with Vegard's law. A pyrochlore phase is observed throughout all compositions studied except the titanate end member, suggesting a low solid solubility of $Nd_2Zr_2O_7$ in $Nd_2Ti_2O_7$. This matches the findings of Shoup et al. [17].

Refinement of biphasic samples proved difficult. A LeBail fit incorporating both phases was necessary to set the lattice and profile parameters at appropriate values. Once a Rietveld analysis was initiated, a good fit was obtained quite quickly. However, it was necessary to constrain thermal parameters of a given type of cation to be the same, in order to obtain a stable refinement. The monoclinic site occupancies for each Zr and Ti atom in the unit cell were fixed at the same values in $Nd_2Zr_{0.8}Ti_{1.2}O_7$ and $Nd_2Zr_{0.4}Ti_{1.6}O_7$, to give refined fractions of cubic and monoclinic phases, respectively, as 0.88 and 0.12 for $Nd_2Zr_{0.8}Ti_{1.2}O_7$ and 0.38 and 0.62, respectively, for $Nd_2Zr_{0.4}Ti_{1.6}O_7$. Using the lever rule, and taking account of the bulk compositions of these two samples, together with the phase fractions of monoclinic and cubic phase in each sample, we can obtain the compositions of these coexisting monoclinic and cubic phases. These are the limiting compositions of solid solubility at the miscibility gap in the $Nd_2(Zr_{1-x}Ti_x)_2O_7$ series. Carrying out this exercise, we find that the most titanium-rich cubic composition (the limit of solid solubility of $Nd_2Ti_2O_7$ in $Nd_2Zr_2O_7$) is $Nd_2Zr_{0.896}Ti_{1.104}O_7$, while the most zirconium-rich monoclinic phase has composition $Nd_2Zr_{0.096}Ti_{1.904}O_7$. In other words, the asymmetric solvus in this system limits the solid solubility of zirconate into the titanate to 4.8 mol% at the monoclinic end, while the limit of titanate into the cubic zirconate is some 55.2 mol%.

The upper radius ratio limit of 1.78 for pyrochlore, discussed earlier, corresponds to a Nd zirconotitanate composition of $Nd_2Zr_{0.3}Ti_{1.7}O_7$, assuming ionic radii of $Nd^{3+} = 1.109$ Å, $Zr^{4+} = 0.72$ Å and $Ti^{4+} = 0.605$ Å from Shannon et al. [23]. This suggests that $Nd_2Zr_{0.3}Ti_{1.7}O_7$ is the absolute compositional limit of solid solution of $Nd_2Ti_2O_7$ in $Nd_2Zr_2O_7$. The fact that a titanate monoclinic phase is observed at the much less Ti-rich composition of $Nd_2Zr_{0.8}Ti_{1.2}O_7$, and that incorporation of $Nd_2Ti_2O_7$ into $Nd_2Zr_2O_7$ stops at this point, according to lattice parameters, is therefore unexpected. This may be attributable to the temperature of sintering. Higher sintering temperatures might lead to enhanced solubility across a wider compositional range for the $Nd_2(Zr_{1-x}Ti_x)_2O_7$ series. The predicted composition at which a monoclinic phase would first be seen, based on the intercept of the trendlines in Fig. 8 is $Nd_2Zr_{0.88}Ti_{1.12}O_7$, which is in very good agreement with the values obtained using the phase fractions described above.

Such behaviour is also suggested by a comparison of the X-ray powder diffraction results from Shoup et al. [17] with our results (Fig. 9). The two data sets show a good overlap across the $Nd_2(Zr_{1-x}Ti_x)_2O_7$ series. However, Shoup reports that a solid solution only exists between 0–43 mol% $Nd_2Ti_2O_7$, compared with 0–56 mol% as indicated by this study. Since the sintering temperatures implemented in the earlier paper are slightly lower than those employed here (1350–1500 °C

Table 3
Refined parameters for monoclinic phases in the series: $Nd_2(Zr_{1-x}Ti_x)_2O_7$, $x = 0.6, 0.8, 1.0$

Atom	x	y	z	B_{iso}/Å^2
$Nd_2Ti_2O_7$ $P2_1$, $R_{wp} = 1.31\%$, $a = 7.6756(1)$ Å, $b = 5.46356(7)$ Å, $c = 25.9964(4)$ Å, $\beta = 98.529(3)^\circ$, volume = 1078.13(3) Å^3				
Nd1	0.278(1)	0.246(2)	0.0481(3)	0.16(8)
Nd2	0.781(1)	0.262(2)	0.0601(3)	0.32(8)
Nd3	0.356(2)	0.656(2)	0.2122(4)	0.7(1)
Nd4	0.852(1)	0.711(1)	0.1916(3)	0.51(9)
Nd5	0.150(2)	0.222(2)	0.3049(4)	1.1(1)
Nd6	0.639(1)	0.157(2)	0.2876(4)	0.4(1)
Nd7	0.221(2)	0.746(2)	0.4425(4)	0.51(8)
Nd8	0.729(2)	0.749(2)	0.4547(4)	1.3(1)
Ti1	0.041(2)	0.740(3)	0.0592(6)	0.1(2)
Ti2	0.533(2)	0.730(4)	0.0560(6)	0.0(1)
Ti3	0.095(4)	0.225(4)	0.1612(7)	0.7(2)
Ti4	0.582(4)	0.205(4)	0.1625(8)	0.4(2)
Ti5	0.413(4)	0.734(4)	0.3419(7)	0.2(1)
Ti6	0.910(3)	0.700(2)	0.3354(5)	0.0(1)
Ti7	0.451(5)	0.254(5)	0.4382(6)	0.9(2)
Ti8	0.972(4)	0.245(4)	0.4397(7)	0.7(2)
O1	0.544(2)	0.477(2)	0.0089(5)	0.0(1)
O2	0.967(2)	0.468(3)	0.0086(6)	0.9(2)
O3	0.292(3)	0.687(4)	0.0548(8)	2.3(2)
O4	0.767(3)	0.822(3)	0.0467(6)	1.3(2)
O5	0.066(2)	0.060(2)	0.0901(4)	0.3(1)
O6	0.534(2)	0.051(2)	0.0937(5)	0.8(1)
O7	0.607(2)	0.538(3)	0.1136(6)	0.9(2)
O8	0.994(2)	0.546(2)	0.1163(6)	0.4(1)
O9	0.328(2)	0.311(3)	0.1493(5)	1.3(1)
O10	0.830(2)	0.172(3)	0.1543(6)	1.4(2)
O11	0.086(2)	0.429(2)	0.2193(5)	0.2(1)
O12	0.633(2)	0.443(2)	0.2159(5)	0.7(2)
O13	0.117(3)	0.933(4)	0.1960(8)	2.7(2)
O14	0.583(2)	0.936(3)	0.2003(5)	1.1(1)
O15	0.382(2)	0.929(2)	0.2851(5)	1.1(2)
O16	0.902(2)	0.918(3)	0.2788(5)	1.2(2)
O17	0.423(1)	0.459(2)	0.2941(4)	0.24(9)
O18	0.875(2)	0.434(2)	0.3043(5)	0.9(2)
O19	0.179(2)	0.653(2)	0.3479(5)	0.6(1)
O20	0.671(2)	0.816(2)	0.3458(3)	0.02(8)
O21	0.382(2)	0.057(3)	0.3874(6)	1.0(2)
O22	0.997(2)	0.061(3)	0.3854(8)	1.4(2)
O23	0.484(2)	0.560(3)	0.4102(6)	1.3(2)
O24	0.930(2)	0.569(3)	0.4091(5)	0.4(2)
O25	0.221(2)	0.327(2)	0.4557(4)	0.25(9)
O26	0.733(2)	0.197(3)	0.4458(6)	0.7(1)
O27	−0.024(2)	0.485(2)	0.5124(5)	1.1(2)
O28	0.540(2)	0.474(3)	0.5121(6)	0.6(1)
$Nd_2Zr_{0.4}Ti_{1.6}O_7$ $P2_1$, $R_{wp} = 1.43\%$, $a = 7.6824(2)$ Å, $b = 5.4690(1)$ Å, $c = 25.9883(8)$ Å, $\beta = 98.489(7)^\circ$, volume = 1079.94(5) Å^3				
Nd1	0.294(2)	0.261(4)	0.0424(6)	2.2(2)
Nd2	0.785(2)	0.268(3)	0.0582(4)	0.4(1)
Nd3	0.357(2)	0.671(4)	0.2140(4)	0.6(1)
Nd4	0.854(2)	0.733(2)	0.1912(3)	0.15(9)
Nd5	0.143(3)	0.207(4)	0.2986(6)	1.8(2)
Nd6	0.632(3)	0.151(4)	0.2898(7)	2.9(3)
Nd7	0.218(2)	0.754(3)	0.4508(5)	1.4(2)
Nd8	0.717(2)	0.767(3)	0.4387(4)	0.4(1)
Zr1/Ti1 0.98(2)	0.023(4)	0.771(4)	0.050(1)	0.07(7)
Zr2/Ti2 0.88(2)	0.537(5)	0.752(6)	0.053(1)	0.07(7)
Zr3/Ti3 0.97(2)	0.082(4)	0.229(5)	0.1615(9)	0.07(7)
Zr4/Ti4 0.94(2)	0.616(3)	0.216(6)	0.159(1)	0.07(7)
Zr5/Ti5 1.00(2)	0.415(4)	0.733(5)	0.3396(8)	0.07(7)

Table 3 (*continued*)

Atom	x	y	z	B_{iso}/Å^2
Zr6/Ti6 0.93(2)	0.925(5)	0.736(5)	0.3365(9)	0.07(7)
Zr7/Ti7 0.95(2)	0.447(3)	0.258(6)	0.4407(7)	0.07(7)
Zr8/Ti8 0.97(2)	0.978(4)	0.264(5)	0.4347(8)	0.07(7)
O1	0.548(2)	0.492(3)	0.0076(6)	0.1(2)
O2	0.967(2)	0.478(4)	0.0108(8)	0.5(2)
O3	0.282(2)	0.706(3)	0.0531(4)	0.0(4)
O4	0.777(2)	0.850(3)	0.0458(5)	0.1(1)
O5	0.089(3)	0.072(4)	0.0922(8)	1.2(2)
O6	0.531(2)	0.069(4)	0.0900(6)	0.5(2)
O7	0.610(2)	0.589(3)	0.1146(6)	0.3(1)
O8	0.993(2)	0.544(3)	0.1147(7)	0.7(2)
O9	0.319(3)	0.329(3)	0.1534(5)	0.6(2)
O10	0.835(3)	0.162(3)	0.1528(5)	0.3(1)
O11	0.083(2)	0.450(4)	0.2183(6)	0.4(2)
O12	0.644(2)	0.447(4)	0.2115(7)	1.0(2)
O13	0.124(2)	0.957(4)	0.1993(6)	0.5(2)
O14	0.578(4)	0.964(5)	0.201(1)	2.0(3)
O15	0.397(3)	0.951(3)	0.2817(6)	0.9(2)
O16	0.889(4)	0.924(3)	0.2777(6)	1.2(2)
O17	0.405(4)	0.472(4)	0.2949(9)	2.4(3)
O18	0.902(4)	0.429(4)	0.3028(7)	1.7(2)
O19	0.190(2)	0.837(4)	0.3485(6)	0.5(2)
O20	0.665(5)	0.690(6)	0.3428(9)	3.1(4)
O21	0.505(3)	0.037(6)	0.3880(9)	2.5(4)
O22	0.902(2)	0.042(4)	0.3764(7)	1.5(3)
O23	0.437(2)	0.587(3)	0.4084(5)	0.4(2)
O24	0.937(3)	0.573(4)	0.4070(7)	0.7(2)
O25	0.230(3)	0.351(4)	0.4561(7)	1.0(2)
O26	0.732(4)	0.253(6)	0.445(1)	3.6(4)
O27	0.048(7)	0.484(9)	0.511(2)	6.7(9)
O28	0.511(7)	0.493(7)	0.507(1)	5.5(5)
$Nd_2Zr_{0.8}Ti_{1.2}O_7$ $P2_1$, $R_{wp} = 2.30\%$, $a = 7.6812(2)$ Å, $b = 5.4677(9)$ Å, $c = 25.998(5)$ Å, $\beta = 98.395(3)^\circ$, volume = 1080.2(4) Å^3				
Nd1	0.26(3)	0.22(4)	0.041(6)	2.2(2)
Nd2	0.77(2)	0.23(4)	0.064(5)	0.4(1)
Nd3	0.36(2)	0.65(4)	0.214(5)	0.6(1)
Nd4	0.84(2)	0.71(4)	0.191(4)	0.15(9)
Nd5	0.15(3)	0.18(5)	0.296(7)	1.8(2)
Nd6	0.64(4)	0.13(5)	0.297(8)	2.9(3)
Nd7	0.21(3)	0.76(5)	0.441(6)	1.4(2)
Nd8	0.71(2)	0.73(4)	0.454(4)	0.4(1)
Zr1/Ti1 0.98(2)	−0.01(4)	0.68(6)	0.05(1)	0.07(7)
Zr2/Ti2 0.88(2)	0.53(5)	0.71(7)	0.07(1)	0.07(7)
Zr3/Ti3 0.97(2)	0.08(4)	0.21(5)	0.154(9)	0.07(7)
Zr4/Ti4 0.94(2)	0.61(4)	0.23(7)	0.15(1)	0.07(7)
Zr5/Ti5 1.00(2)	0.41(4)	0.69(5)	0.334(8)	0.07(7)
Zr6/Ti6 0.93(2)	0.97(4)	0.69(8)	0.34(1)	0.07(7)
Zr7/Ti7 0.95(2)	0.44(4)	0.23(7)	0.44(1)	0.07(7)
Zr8/Ti8 0.97(2)	0.99(4)	0.26(7)	0.43(1)	0.07(7)
O1	0.56(2)	0.45(5)	0.015(5)	0.1(2)
O2	0.97(2)	0.46(5)	0.007(7)	0.5(2)
O3	0.26(2)	0.68(4)	0.046(5)	0.0(4)
O4	0.77(2)	0.81(4)	0.049(6)	0.1(1)
O5	0.06(3)	0.02(6)	0.091(9)	1.2(2)
O6	0.54(2)	0.06(5)	0.090(7)	0.5(2)
O7	0.60(2)	0.55(5)	0.119(7)	0.3(1)
O8	0.98(2)	0.47(5)	0.113(8)	0.7(2)
O9	0.32(3)	0.30(5)	0.159(6)	0.6(2)
O10	0.83(3)	0.14(5)	0.157(6)	0.3(1)
O11	0.09(2)	0.41(5)	0.215(6)	0.4(2)
O12	0.63(3)	0.43(5)	0.217(8)	1.0(2)
O13	0.14(2)	0.94(5)	0.204(6)	0.5(2)
O14	0.61(3)	0.95(6)	0.214(9)	2.0(3)

Table 3 (*continued*)

Atom	x	y	z	B_{iso}/Å^2
O15	0.38(3)	0.92(5)	0.285(7)	0.9(2)
O16	0.91(3)	0.90(5)	0.281(8)	1.2(2)
O17	0.42(4)	0.45(6)	0.296(9)	2.4(3)
O18	0.91(4)	0.44(5)	0.296(8)	1.7(2)
O19	0.18(3)	0.75(5)	0.337(5)	0.5(2)
O20	0.66(4)	0.68(6)	0.34(1)	3.1(4)
O21	0.48(5)	0.07(5)	0.386(9)	2.5(4)
O22	0.97(3)	0.01(5)	0.377(8)	1.5(3)
O23	0.48(3)	0.52(5)	0.402(6)	0.4(2)
O24	0.97(3)	0.55(5)	0.398(6)	0.7(2)
O25	0.21(3)	0.29(6)	0.435(7)	1.0(2)
O26	0.69(5)	0.26(7)	0.45(1)	3.6(4)
O27	0.00(9)	0.44(7)	0.48(1)	6.7(9)
O28	0.46(5)	0.49(7)	0.50(1)	5.5(5)

Figures are shown in the first column for Zr and Ti sites giving the fraction of Ti on the site (= 1–fraction Zr).

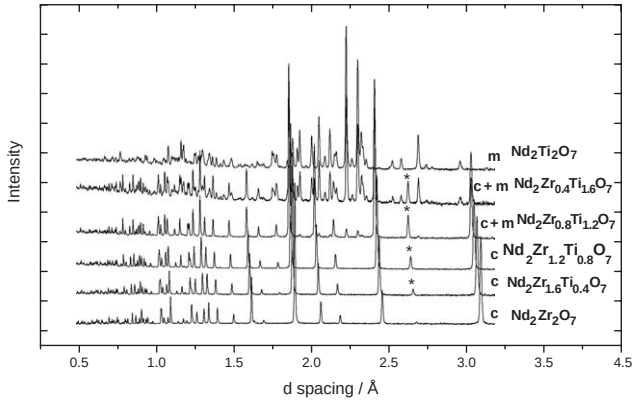

Fig. 6. TOF neutron powder diffraction patterns for the compositional series: $Nd_2(Zr_{1-x}Ti_x)_2O_7$. Ideal stoichiometric compositions are given. The phases present in each diffraction pattern are indicated by c = cubic pyrochlore (space group $Fd\bar{3}m$) and m = monoclinic (space group = $P2_1$). The (400) pyrochlore peak is indicated by '*'.

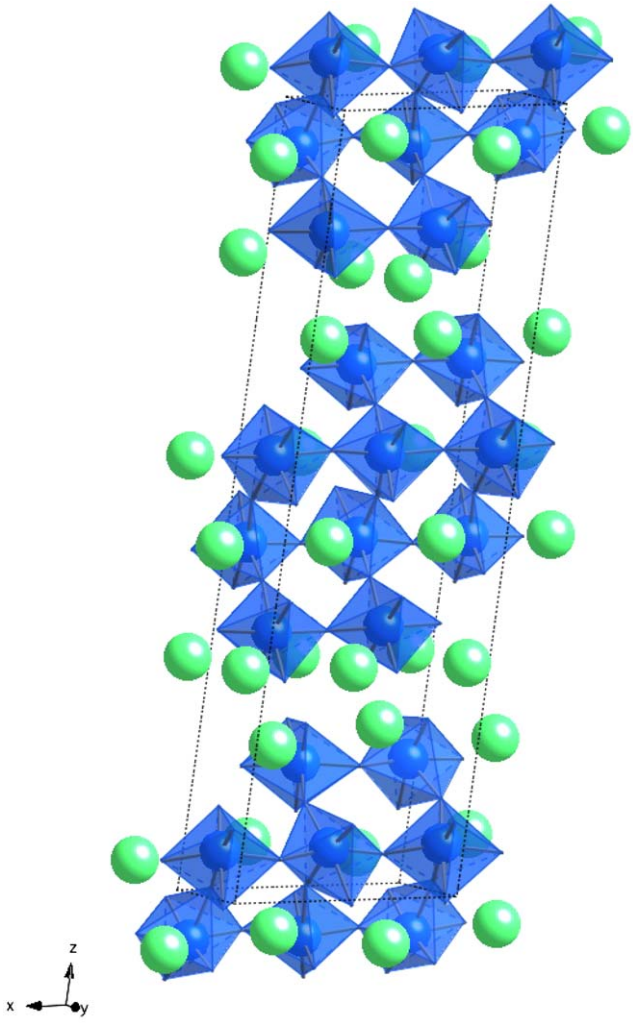

Fig. 7. Monoclinic structure formed at high proportions of Ti in $Nd_2(Zr_{1-x}Ti_x)_2O_7$. The unit cell is outlined in black. Nd ions are shown as light coloured (green online) spheres. The grey (blue online) polyhedra indicate 6-fold coordination of oxygen atoms around Zr and Ti atoms.

compared to 1500 °C throughout), this seems to support a temperature dominated effect on the magnitude of solid solubility. Detailed inspection of Shoup's results suggests that the degree of solid solution may be more extensive than that quoted—it may even be as high as 57 mol% $Nd_2Ti_2O_7$—a value much closer to that reported here.

It is interesting to note, that whilst the lattice parameters and bond lengths follow the same overall trends for both the $(La_{1-x}Nd_x)_2Zr_2O_7$ and $Nd_2(Zr_{1-x}Ti_x)_2O_7$ series, the 48*f* x-parameter shows different behaviour—it increases for $(La_{1-x}Nd_x)_2Zr_2O_7$ (Fig. 4b) and decreases for $Nd_2(Zr_{1-x}Ti_x)_2O_7$ (Fig. 10). One possible explanation for this employs electronegativity arguments in conjunction with a discussion of ionic radii. The Pauling electronegativity of Ti (1.32) is greater than that of Zr (1.22). Ti^{4+} is also much smaller than Zr^{4+} (0.605 Å compared to 0.72 Å [24]). The resulting increase in Coulombic attraction and reduction in equilibrium bond distance, forces the six surrounding 48*f* oxygens to be attracted towards the nearest 16*c* site to a greater extent, which affects their ability to relax towards vacant 8*a* sites in the pyrochlore structure (Fig. 1b) and leads to a reduction in the 48*f* oxygen x-parameter. For $(La_{1-x}Nd_x)_2Zr_2O_7$, as the proportion of Nd is raised, the average size of the A cations decrease. The oxygen ions surrounding 16*d* sites (including 6 48*f* oxygens) move towards the smaller A cations, occupying positions closer to that of oxygen ions in fluorite. As a result, the 48*f* oxygen x-parameter increases. This effect outweighs the small decrease in electronegativity due to replacing La with Nd, which would work in the opposite direction (Pauling electronegativities of $La^{3+} = 1.08$, $Nd^{3+} = 1.07$). As with $(La_{1-x}Nd_x)_2Zr_2O_7$, cation

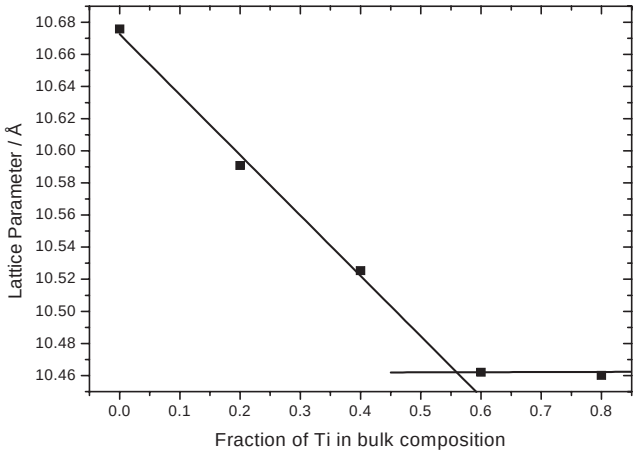

Fig. 8. Cubic lattice parameters for $Nd_2(Zr_{1-x}Ti_x)_2O_7$. Error bars are smaller than the size of the symbols. Two trendlines are displayed. The first outlines the range of compositions over which Vegard's law is satisfied. The second indicates the compositions studied where the limit of $Nd_2Ti_2O_7$ solubility in $Nd_2Zr_2O_7$ has been exceeded. The intercept of these trendlines falls at $x = 0.56$ and indicates the limit of Ti incorporation into an $Nd_2(Zr_{1-x}Ti_x)_2O_7$ pyrochlore solid solution under the synthesis conditions employed.

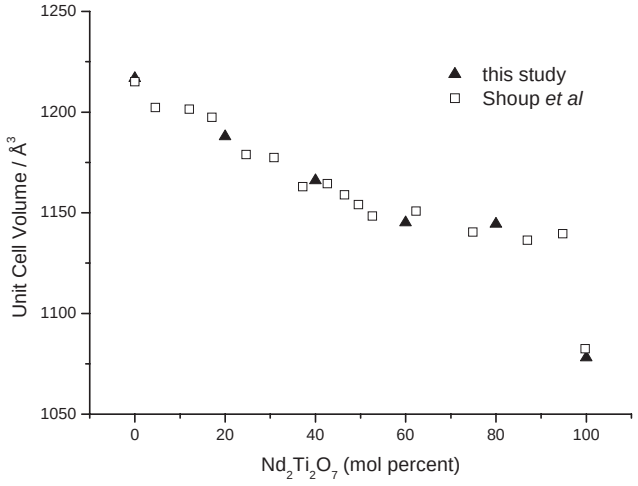

Fig. 9. Unit cell volumes for the series $Nd_2(Zr_{1-x}Ti_x)_2O_7$. Values are obtained from data fitting of cubic phases with the exception of those for $Nd_2Ti_2O_7$, which exists as a single, monoclinic phase.

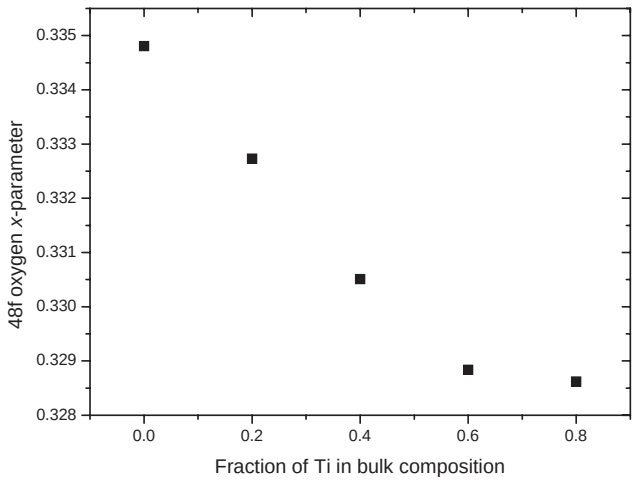

Fig. 10. 48*f* oxygen *x*-positional parameter for pyrochlore phases in the series $Nd_2(Zr_{1-x}Ti_x)_2O_7$. Error bars are smaller than the size of the symbols.

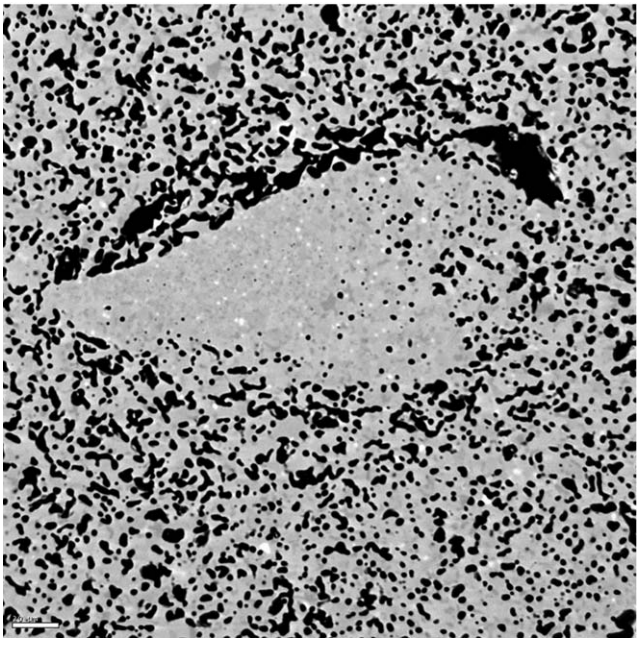

Fig. 11. Backscattered SEM image of sample with bulk composition $Nd_2Zr_{0.8}Ti_{1.2}O_7$. Note the light grey matrix containing dark grey regions. White spots are localised Si impurities incorporated during synthesis. Black areas are pores in the sample. Scale bar is 20 μm.

disorder across the *A* and *B* sites may explain the non-linear behaviour of the 48*f* oxygen *x*-parameter.

Backscattered scanning electron (BSE) microscopy is a very powerful technique for elucidating phase types and compositional variations, particularly when used in conjunction with powder diffraction patterns. Since Zr and Ti have very different electron densities, localised regions of varying composition scatter the incoming electron beam to different extents (Zr more than Ti). Ti rich areas (monoclinic) appear dark and can therefore be distinguished from lighter, Zr rich regions (pyrochlore). This is illustrated in Fig. 11, which shows the $Nd_2Zr_{0.8}Ti_{1.2}O_7$ sample. As indicated by the diffraction patterns discussed above, the majority of the sample is composed of cubic pyrochlore, but a titanate rich monoclinic phase has begun to exsolve. This appears as isolated dark spots, comprising approximately 20% of the ceramic matrix. EDS confirms this interpretation—these dark regions contain very little Zr, and are rich in Ti. The lighter regions, which comprise most of the sample have a much higher proportion of Zr.

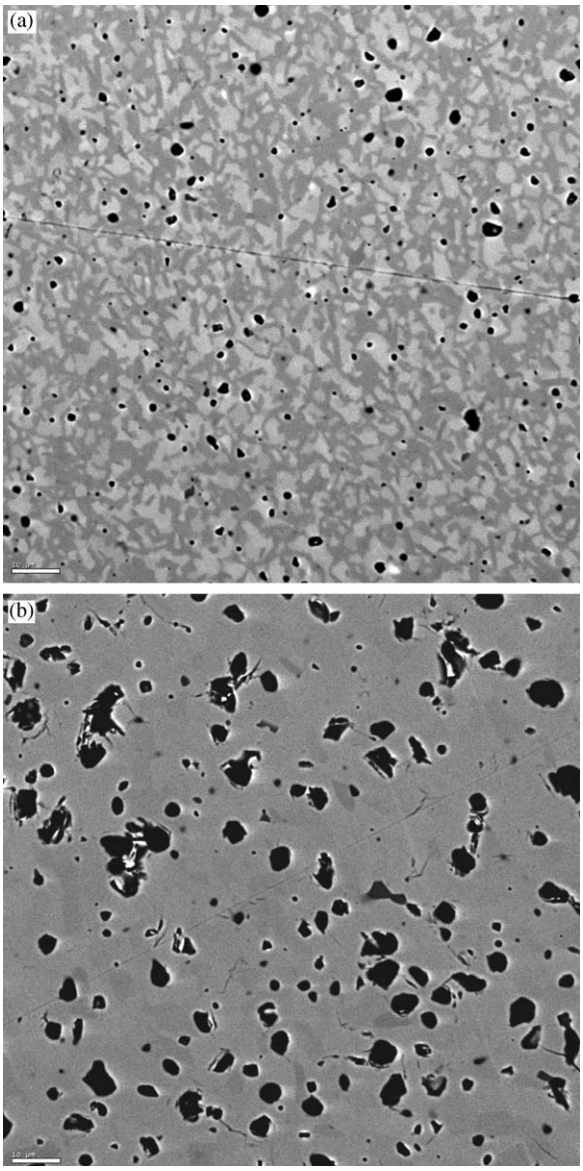

Fig. 12. Backscattered SEM images of samples with bulk composition (a) $Nd_2Zr_{0.4}Ti_{1.6}O_7$ and (b) $Nd_2Ti_2O_7$. Scale bars are 10 μm.

Localised Si impurities, probably incorporated during synthesis procedures are also apparent (white spots in micrograph).

Once the proportion of Ti is raised to give an overall composition of $Nd_2Zr_{0.4}Ti_{1.6}O_7$, it can be seen (Fig. 12a) that the two crystalline phases coexist in an interconnecting manner, in approximately equal proportions. The same compositional distribution is suggested by the EDS results for this sample as for the phases observed in $Nd_2Zr_{0.8}Ti_{1.2}O_7$.

Given the apparent proportions of the two phases present in the BSE images of the $Nd_2Zr_{0.4}Ti_{1.6}O_7$ sample, it is worth noting that if the vast majority of the Zr present partitions into pyrochlore preferentially, a 50% proportion of monoclinic titanate phase would cause the proportion of Zr in the cubic phase to be about twice that of the bulk stoichiometry. This is indeed observed: the refined fractional 16*c* site occupancy for $Nd_2Zr_{0.4}Ti_{1.6}O_7$ given in Table 2 is $Zr = 0.445$—more than double the bulk value of 0.2. This further supports the suggestion of a low solid solubility of $Nd_2Zr_2O_7$ in $Nd_2Ti_2O_7$.

A much more uniform backscattered SEM picture is observed for $Nd_2Ti_2O_7$ (Fig. 12b), as expected from the single phase nature of this material. Some localised darker regions can be seen. However, any differences in contrast are far less pronounced and EDS shows no compositional differences. It seems likely that there is some very slight zoning of elements within this sample, which gives rise to areas that appear slightly darker in the backscattered SEM.

By comparison of the micrographs displayed here (Figs. 5, 11 and 12), it can be seen that the sintered quality of samples improves drastically as the proportion of Ti in the bulk composition is increased. As the composition approaches the titanate end member, pore spaces become smaller and less interconnected. This occurs because the melting point of TiO_2 is substantially lower than that of ZrO_2, so that coalescence and sintering of particles is more easily facilitated. It explains the large reduction in external dimensions observed for sintered pellets containing a high proportion of Ti.

4. Conclusions

Oxides of the form $(La_{1-x}Nd_x)_2Zr_2O_7$ and $Nd_2(Zr_{1-x}Ti_x)_2O_7$ were synthesized by mixed metal-oxide methods and studied by powder neutron diffraction and backscattered scanning electron microscopy coupled with energy dispersive spectroscopy. The first series retained a pyrochlore structure throughout, displaying a linear decrease in lattice parameter, from 10.8047 to 10.6758 Å. The 48*f* oxygen *x*-parameter also behaves linearly, increasing from 0.3313 to 0.3348 with increasing Nd-content. The latter change in value corresponds to an increasing distortion of 6 coordinate 16*c* sites and decreasing distortion of 8 coordinate 16*d* sites to a geometry approaching cubic. BSE images confirm a uniform, single phase sample.

For the series $Nd_2(Zr_{1-x}Ti_x)_2O_7$, partial solid solubility was observed, up to an approximate value of $x = 0.56$. At lower x values, a single pyrochlore phase formed, again with a linear decrease in lattice parameter, this time with increasing Ti-content. The limit of solid solubility was indicated by the exsolution of a titanate rich monoclinic phase, observed in both powder diffraction and BSE images. The cubic pyrochlore phase existed with the monoclinic Ti-rich phase in all samples with $x > 0.56$ except the titanate end member, suggesting a low solubility of Zr in $Nd_2Ti_2O_7$.

Results obtained from pattern profile refinements show similar trends to those obtained previously by Shoup et al. [17]. However, the difference in solid solubility limits observed between the two datasets, coupled with the deviation from the theoretical limit of solid solubility ($Nd_2Zr_{0.3}Ti_{1.7}O_7$), suggests that temperature has a strong effect on the observed region of solid solution. The ability of Zr and Ti to coexist in rare-earth zirconotitanate pyrochlores, together with the likely resistance of such materials to radiation damage and groundwater attack make zirconotitanates strong candidates for the immobilisation of highly active actinide species from radioactive waste.

Acknowledgments

The authors gratefully acknowledge support from the Engineering and Physical Sciences Research Council (EPSRC), British Nuclear Fuel Ltd. (BNFL) and the Cambridge Massachusetts Institute (CMI). We are also grateful to the Council for the Central Laboratory of the Research Councils (CCLRC) for the award of neutron beam time at ISIS, Rutherford Appleton Laboratory.

References

[1] A.E. Ringwood, Safe disposal of high level nuclear reactor wastes: a new strategy, Australian National University Press, Canberra, 1978.
[2] J.C. Malmstrom, Zirconolite: Experiments on the Stability in Hydrothermal Fluids, Dissertation 13717, ETH, Zurich, (2000).
[3] B.B. Ebbinghaus, G.A. Armantrout, L. Gray, C.C. Herman, H.F. Shaw, R.A. Van Konynenburg, Plutonium Immobilization Project Baseline Formulation, UCRL-ID-133089, rev. 1, PIP-00-141, 2000.
[4] B.B. Ebbinghaus, R.A. Van Konynenburg, E.R. Vance, M.W. Stewart, A. Jostsons, J.S. Allender, D.T. Rankin, Ceramic Composition for Immobilization of Actinides, US Patent 6,137,025, 1999.
[5] M.A. Subramanian, G. Aravamundan, G.V. Subba Rao, Oxide Pyrochlores—A Review, Prog. Solid St. Chem. 15 (1983) 55–143.
[6] R.E. Carbonio, J.A. Alonso, J.L. Martínez, Oxygen vacancy control in the defect $Bi_2Ru_2O_{7-y}$ pyrochlore: a way to tune the electronic bandwidth, J. Phys.: Condens. Matter 11 (1999) 55–143.
[7] R. Vassen, X. Cao, F. Tietz, D. Basu, D. Stover, Zirconates as new materials for thermal barrier coatings, J. Am. Ceram. Soc. 83 (2000) 2023–2028.
[8] J.E. Greedan, Geometrically frustrated magnetic materials, J. Mater. Chem. 11 (2001) 37–53.
[9] M. Langlet, C. Coutier, J. Fick, M. Audier, W. Meffre, B. Jacquier, R. Rimet, Sol–gel thin film deposition and characterization of a new optically active compound: $Er_2Ti_2O_7$, Opt. Mater. 16 (2001) 463–473.
[10] J.A. Fortner, A.J. Kropf, R.J. Finch, A. J Bakel, M.C. Hash, D.B. Chamberlain, Crystal chemistry of uranium (V) and plutonium (IV) in a titanate ceramic for disposition of surplus fissile material, J. Nucl. Mater. 304 (2002) 56–62.
[11] S.S. Shoup, C.E. Bamberger, R.G. Haire, Novel plutonium titanate compounds and solid solutions $Pu_2Ti_2O_7$–$Ln_2Ti_2O_7$: relevance to Nuclear Waste Disposal, J. Am. Ceram. Soc. 79 (1996) 1489–1493.
[12] G.R. Lumpkin, Alpha-decay damage and aqueous durability of actinide host phases in natural systems, J. Nucl. Mater. 289 (2001) 136–166.
[13] J. Lian, X.T. Zuk, V.G. Kutty, J. Chen, L.M. Wang, R.C. Ewing, Ion-irradiation-induced amorphization of $La_2Zr_2O_7$ pyrochlore, Phys. Rev. B 66 (2002) 54108-1–54108-5.
[14] S.X. Wang, L.M. Wang, R.C. Ewing, K.V. Govindan Kutty, Ion irradiation of rare-earth and yttrium-titanate-pyrochlores, Nucl. Instrum. Meth. B 169 (2000) 135–140.
[15] S.X. Wang, B.D. Begg, L.M. Wang, R.C. Ewing, W.J. Weber, K.V. Govindan Kutty, Radiation stability of gadolinium zirconate: a waste form for plutonium disposition, J. Mater. Res. 14 (12) (1999) 4470–4473.
[16] M.W.A. Stewart, B.D. Begg, E.R. Vance, K. Finnie, H. Li, G.R. Lumpkin, K.L. Smith, W.J. Weber, S. Thevuthasan, The replacement of titanium by zirconium in ceramics for plutonium immobilization, Mater. Res. Soc. Symp. Proc. 713 (2002) JJ2.5.1–JJ2.5.8.
[17] S.S. Shoup, C.E. Bamberger, J.L. Tyree, L.M. Anovitz, Lanthanide-containing zirconotitanate solid solutions, J. Solid State Chem. 127 (1996) 231–239.
[18] R.I. Smith, S. Hull, User Guide for the Polaris Powder Diffractometer at ISIS, CCLRC Technical Report, RAL-TR-97-038, 1997.
[19] H.M. Rietveld, A profile refinement method for nuclear and magnetic structures, J. Appl. Crystallogr. 2 (1969) 65–71.
[20] A.C. Larson, R.B. Von Dreele, General structure analysis system, Los Alamos National Laboratory Report LAUR (2001) 86–748.
[21] B.H. Toby, EXPGUI, a graphical user interface for GSAS, J. Appl. Crystallogr. 34 (2001) 210–213.
[22] Y. Tabira, R.L. Withers, The determination of an unknown oxygen atom position in rare-earth zirconate pyrochlores by a 111 systematic row CBED technique, Philos. Mag. A 79 (1999) 1335–1346.
[23] C. Heremans, B.J. Wuensch, J.K. Stalick, E. Prince, Fast-Ion Conducting $Y_2(Zr_yTi_{1-y})_2O_7$ Pyrochlores: neutron rietveld analysis of disorder induced by Zr substitution, J. Solid State Chem. 117 (1995) 108–121.
[24] R.D. Shannon, Revised effective ionic radii and systematic studies of interatomic distances in halides and chalcogenides, Acta Crystallogr. A 32 (1976) 751–767.
[25] Y. Tabira, R.I. Withers, T. Yamada, N. Ishizawa, Annular dynamical disorder of the rare earth ions in a $La_2Zr_2O_7$ pyrochlore via single crystal synchrotron X-ray diffraction, Zeitschrift für Kristallographie 216 (2001) 92–98.
[26] K.R. Whittle, G.R. Lumpkin, S.A.T. Redfern, I. Swainson, R.I. Smith, Structural studies of lanthanide pyrochlores and the effect of yttrium addition, J. Solid State Chem. (2004) submitted.
[27] M.P. van Dijk, J.H.H. Ter Maat, G. Roelofs, H. Bosch, G.M.H. van de Velde, P.J. Gellings, A.J. Burggraaf, Electrical and catalytic properties of some oxides with the fluorite or pyrochlore structure. Part I: synthesis, characterization and conductivity, Mater. Res. Bull. 19 (1984) 1149–1156.
[28] L. Minervini, R.W. Grimes, Y. Tabira, R.L. Withers, K.E. Sickafus, The oxygen positional parameter in pyrochlores and its dependence on disorder, Philos. Mag. A 82 (2002) 123–135.
[29] L. Minervini, R.W. Grimes, K.E. Sickafus, Disorder in pyrochlore oxides, J. Am. Ceram. Soc. 83 (2000) 1873–1878.